Effects of Ink Formulation on Constructing Catalyst Layers

for High-Performance PEM Fuel Cells

Qing Gong[1,2], Chenzhao Li[1,3], Jan Ilavsky[4], Fei Guo[5], Xuan Cheng[2]*, Jian Xie[1]*

[1] Department of Mechanical Engineering, Purdue School of Engineering and Technology, Indiana University-Purdue University, Indianapolis, Indiana 46202, USA. Email: jianxie@iupui.edu

[2] Department of Materials Science and Engineering, College of Materials, Xiamen University, Xiamen, Fujian 361005, China.

[3] School of Mechanical Engineering, Purdue University, West Lafayette, Indiana 47906, USA

[4] X-Ray Science Division, Argonne National Laboratory, Lemont, Illinois 60439, USA

[5] Department of Molecular and Cellular Biology, University of California, Davis, Davis, CA 95616-8665, USA

Key words: Pt/C catalyst, catalyst layer, PEMFC, ink formulation, MEA fabrication,

---

Abstract

Rational design of the catalyst layers in a membrane electrode assembly (MEA) is crucial for achieving high-performance proton exchange membrane (PEM) fuel cells. Establishing a clear understanding of the property (catalyst ink)-structure (catalyst layer)-performance (MEA) relationship lays the foundation for this rational design. In this work, a synergistic approach was taken to correlate the ink formulation, the microstructure of catalyst layers, and the resulted MEA performance to establish such a property-structure-performance relationship. The solvent composition (n-PA/H_2O mixtures) demonstrated a strong influence on the MEA performance, especially polarization losses of cell activation and mass-transport. The performance differences were studied in terms of how the solvent composition affects the catalyst/ionomer interface, ionomer network, and pore structure of the resulting catalyst layers. The ionomer aggregates mainly covered on the surface of catalyst aggregates acting as ORR active sites, and the aggregate sizes of ionomer and catalyst (revealed by USAXS and cryo-TEM) were dictated by tuning the solvent composition, which in turn determined the catalyst/ionomer interface (available active sites). In n-PA/H_2O mixtures with 50~90 wt.% H_2O, the catalyst agglomerates could be effectively breakup into small aggregates, leading to enhanced kinetic activities. The boiling point of the mixed solvents determined the pore structure of ultimate catalyst layers, evidenced by the mercury porosimetery and SEM. For mixed solvent with a higher boiling point, the catalyst-ionomer aggregates in the ink tend to agglomerate during the solvent evaporation process and finally form larger catalyst-ionomer aggregates in ultimate catalyst layer, resulting in more secondary pores and thus lower mass transport resistance. Both the enlarged catalyst/ionomer interface and

appropriate pore structure were achieved with the catalyst layer fabricated from n-PA/H_2O mixture

with 90 wt.% H_2O, leading to the best MEA performance.

Introduction

Proton exchange membrane (PEM) fuel cells are an attractive technology for energy conversion with advantages of high efficiency and low emission. As being driven toward commercialization, the focus of PEM fuel cells research and development has been shifted on reducing cost and improving performance. The cathode catalyst layer in a membrane electrode assembly (MEA), at which oxygen reduction reaction (ORR) takes place, is a key component of PEM fuel cells. Catalyst layers are usually formed by depositing and solidifying a catalyst ink, which consists of catalyst powder, ionomer and dispersing solvent, onto gas diffusion layer or membrane. An ideal catalyst layer needs to have maximized catalyst/ionomer interface as reaction sites for ORR, good ionomer network for proton conduction, and appropriate pore structure to facilitate mass transport of reactant gases and product water. The microstructure of a catalyst layer depends on the catalyst ink, particularly, the dispersion of catalyst powder and ionomer particles in a solvent system, which determine the catalyst/ionomer interface, ionomer network, and pore structure of the resulting catalyst layer.

Effective ink formulation is necessary to break up the large agglomerates of catalyst and ionomer to achieve the desired particle size and ink viscosity for different coating methods. The physical properties of dielectric constant, and solubility for a dispersing solvent dominate the size and morphology of the two dispersed components (catalyst and ionomer) in the ink.[1-10] The dielectric constant of a solvent is closely related to its polarizability, which affects the solubility and dispersibility of the solvent to the molecules/ions of another substance. An early study demonstrated that, depending on the dielectric constant (ε) of different solvents, Nafion ionomer

in a solvent could form one of three states: solution ($\varepsilon > 10$), colloid ($3 < \varepsilon < 10$), and precipitation ($\varepsilon < 3$).[1] Since then, extensive organic solvents with different dielectric constants were studied for catalyst layer fabrication.[3-4, 11-15] Two most commonly used MEA fabrication techniques are gas diffusion electrode (GDE) and catalyst-coated membrane (CCM). The CCM can be fabricated using different techniques, such as decal transfer method, hand-painting, machine spraying/coating, screen-printing, etc. Shin et al. compared the MEAs fabricated with a colloid-type solvent of n-butyl acetate ($\varepsilon = 5.01$) and a solution-type solvent of isopropanol ($\varepsilon = 18.3$) using GDE method.[11] The MEA fabricated with a colloid-type solvent of n-butyl acetate exhibited an improved performance due to the continuous ionomer network and porous structure of the catalyst layer. Fernandez et al. studied a series of solution-type organic solvents ($16.5 < \varepsilon < 74.9$) using the same fabrication method, and their results indicated that the MEA performance could be enhanced with a lower dielectric constant solvent.[12] However, these findings regarding dielectric constant contradict the conclusions of other studies, especially those using CCM methods.[3-4, 13-15] Other physical properties of a dispersing solvent, particularly the viscosity and boiling point play a vital role in the subsequent coating and evaporation steps, thus affecting the microstructure of the resulting catalyst layer.[12, 14-20] Depending on the coating method, viscous inks are preferred for brushing, rod coating and doctor blade spreading, while thinner inks are suitable for spraying method. The solvent needs to be removed through evaporation during or after the coating process to form a dry and porous catalyst layer, and the evaporation rate, which is closely related to the boiling point of a dispersing solvent, was considered to be related to the pore structure of the ultimate catalyst layer.[15-18] However, it is not clear how the boiling point affects the pore structure.

Although these studies on solvent properties are very insightful, they mainly focus on a particular topic, approach or direction. A comprehensive study is needed on the effect of the MEA performance from the various factors in fabricating the catalyst layer.

Currently, the mixed solvents of alcohol and water, especially isopropanol (i-PA)/H_2O and n-propanol (n-PA)/H_2O mixtures, are the most common solvents used for catalyst ink preparation. Several research groups optimized the composition of mixed solvents using different MEA fabrication techniques.[3-4, 19, 21-24] The optimum composition varied significantly in different studies due to the differences in many parameters including materials and fabrication techniques used. For catalyst layers prepared though CCM method using commercial 50 wt.% Pt/C and traditional Nafion (1100-EW) ionomer, the optimum composition of n-PA/H_2O mixed solvents was found to be ~60 wt.% H_2O.[21-22] However, using the same Nafion ionomer and CCM method, the optimum composition of n-PA/H_2O mixed solvents became 82 wt.% H_2O for commercial Fe-N-C catalyst.[19] Based on i-PA/H_2O mixed solvents, the best MEA performance was achieved with 80 wt.% H_2O using commercial 38 wt.% Pt/C and Nafion ionomer through GDE method.[3] Low-EW (equivalent weight) ionomers have great advantage in proton conduction over traditional Nafion ionomer, thus improving MEA performance.[25] However, only one study on solvent optimization was based on low-EW ionomer.[23] For catalyst layers prepared though GDE method using commercial 46.9 wt.% Pt/C and low-EW (700-EW) ionomer, the optimum composition of n-PA/H_2O mixed solvents was reported to be 16 wt.% H_2O. Obviously, this alcohol-rich composition seriously deviated the optimum composition (H_2O-rich) in other studies. This could be attributed to the use of low EW ionomer and ultra-high catalyst concentration (~94 mg·mL^{-1}) in this study. Although great efforts

have been made to obtain a good catalyst ink for MEA fabrication, a clear understanding of the property (ink)-structure (catalyst layer)-performance (MEA) relationship is still lacking.

This work aims to establish a property (ink)-structure (catalyst layer)-performance (MEA) relationship toward the efficient design of best-performing electrodes. A series of MEAs were fabricated using CCM method from catalyst inks obtained by dispersing commercial 20 wt.% Pt/C catalyst and low-EW (830-EW) ionomer in n-PA/H_2O mixed solvents with various compositions. The effects of solvent composition on the dispersion of catalyst and ionomer particles, the microstructure of catalyst layers, and MEA performance were systematically investigated.

Experimental Section

Catalyst Ink Preparation. Catalyst inks were prepared by dispersing commercial 20 wt.% Pt/C (E-TEK) and 6 wt.% ionomer solution (Aquivion, 830-EW) in different n-PA/H_2O mixed solvents. A total of 6 catalyst inks, in which the n-PA/H_2O mixed solvents containing 0, 20, 50, 70, 90, and 100 wt.% H_2O was used for the fabrication of cathode catalyst layers. The n-PA/H_2O mixed solvent with 50 wt.% H_2O was used for anode catalyst layer preparation. For all catalyst inks, the weight ratio of ionomer to carbon was controlled to 0.45. Before spraying, all catalyst inks were homogenized using an ultrasonic bath for 60 min.

MEA Fabrication. The catalyst inks were ultrasonically sprayed onto Nafion-212 membranes using an ExactCoat spray coating system (Sono-Tek, NY). For both anode and cathode catalyst layers, the Pt loadings were controlled to be 0.10 ± 0.02 mg·cm^{-2} by weighing the Nafion membrane before and after coating. The CCMs were sandwiched by two gas diffusion layers

(Sigracet 29BC, SGL Global, Germany) without hot pressing.

Fuel Cell Testing. The MEA was assembled into a fuel cell hardware with an active area of 5.0 cm^2, and tested on a model 850e fuel cell test system (Scribner Associates, Inc., NC). The cell temperature was maintained to be 80 °C, and the gases were humidified at 80 °C, throughout the tests. The MEA was activated (break-in) using potential step mode from 0.35 to 0.75 V in 0.05 V increments every 5 min for 16 hours with H$_2$/air flowrates of 200/400 standard cubic centimeter per minute (sccm). After break-in, the electrochemical active surface area (ECSA) was determined using the electrochemical hydrogen adsorption method by employing a cyclic voltammetry (CV) between 0.05 and 0.60 V with a scan rate of 20 mV·s^{-1} under 100 kPa (absolute). Prior to ECSA measurement, the cathode side was purged with N$_2$ until the open circuit voltage (OCV) dropped to below 0.15 V. The CV measurement was carried out using an electrochemical workstation (Solartron 1287BZ, AMETEK, PA).

Fuel cell polarization curves were recorded using potential step mode with 50 mV/point (holding 1 min at each point). The H$_2$/O$_2$ polarization curves were recorded with anode/cathode flowrates of 200/400 sccm under 150 kPa (absolute) backpressure. The cell resistance was monitored during the acquisition of polarization curves using the current interrupt method. The iR-corrected polarization curves were used for analyzing the characteristics of kinetic activity and mass transport. Mass activities were reported at 0.90 V after applying iR corrections. The H$_2$/air polarization curves were measured at a constant H$_2$/air flowrate of 500/2000 sccm under 150 kPa (absolute) backpressure. The electrochemical impedance spectroscopies were collected at 1.0 A·cm^{-2} by scanning frequency from 10^4 Hz to 0.1 Hz.

Ultrasmall Angle X-ray Scattering. The X-ray scattering measurements were conducted at beamline 9ID-C at the Advanced Photon Source (APS), Argonne National Laboratory. The samples after sonication were collected into a glass capillary tube (1 mm diameter) and sealed with a rubber cap. The sample tubes were mounted in the beamline hutch and exposed to a monochromatic X-ray beam in the range of 10~24 keV. The scattered intensity was collected within a scattering vector range of 10^{-4} to 1 Å^{-1} by using a Bonse-Hart camera setup for USAXS and a Pilatus 100 K detector for pinhole SAXS. The background scattering data from the capillary tube filled with the corresponding solvent (n-PA/H_2O) was recorded and subtracted from scattering data for each corresponding catalyst ink. The scattering data were analyzed in a modeling macro package Irena for data fitting and simulation on Igor Pro (WaveMetrics, OR) platform.

Cryo-TEM Analysis. A 3.5 uL aliquot of the sample was placed on a copper grid (400 mesh) coated with holey carbon film. The excess sample was blotted with filter paper. The grid was then immediately plunged into liquid ethane cooled by liquid nitrogen. The sample grid was loaded into the microscope with a Gatan side-entry cryo-holder. Low-dose images were collected using CM200 or CM300 cryo-microscope with a field emission gun operating at 200 or 300 kV, respectively.

Mercury Porosimetery. The pore size and specific pore volume distributions in the catalyst layers were measured using an Autopore IV 9520 mercury porosimeter (Micromeritics, Norcross, GA). Catalyst layer coated Nafion-212 membrane was cut into strips, and then used for mercury intrusion porosimetry test. During the testing, mercury was intruded into the porous catalyst layer progressively by applying an external pressure from 0.25 psia to 60000 psia with an equilibration

time of 10 s. The pore size was determined by using the Washburn equation, which establishes a direct relationship between the external pressure and the pore diameters.

Scanning Electron Microscope. The surface and cross-section morphology of the catalyst layers were characterized using JEOL-7800 field emission scanning electron microscope (FESEM) (JEOL USA, MA). The fresh catalyst layer coated Nafion-212 membrane was cut in liquid nitrogen, and then used for microscopic tests.

Results and discussion

The H_2/O_2 performances of MEAs fabricated with different H_2O contents in ink solvents are presented in Figure 1(a). Obviously, the H_2O content has a significant effect on the MEA performance. The MEA fabricated with 90 wt.% H_2O demonstrated the best performance over the entire polarization range. The ohmic resistances remained almost unchanged with different H_2O contents, as evidenced by the severely overlapping iR drop curves at the bottom of Figure 1(a). As is well-known, the MEA performance is dominated by polarization losses of kinetic activation, ohmic resistance and mass transport. Therefore, the performance differences in this study could be mainly attributed to different oxygen reduction reaction (ORR) kinetics and mass transport limitations of these MEAs. In Figure 1(a), minor performance differences are observed at high cell voltages (>0.8 V). To further interpret the ORR kinetics of different MEAs, Tafel plots are constructed in Figure 1(b). The Tafel slopes and mass activity (MA) values at 0.9 $V_{iR\text{-free}}$ are summarized in Table I. The Tafel slopes of MEAs was between 63.9 and 71.0 mV·dec^{-1}, which are close to the theoretical value of 70 mV·dec^{-1}.(26) The mass activity varied from 140.2 to 189.4

mA·mg$_{Pt}^{-1}$ with the alteration of H$_2$O content. Mass activity and electrochemical surface area (ECSA) are practical indicators for evaluating the kinetic activity of different catalyst layers, which are compared in Figure 1(c). Obviously, the mass activity significantly improved with increasing the H$_2$O content from 0 to 90 wt.% H$_2$O. The MEA with 90 wt.% H$_2$O delivered the highest mass activity of 189.4 mA·mg$_{Pt}^{-1}$, close to that obtained in the rotating disc electrode (RDE) (197.8 mA·mg$_{Pt}^{-1}$, Figure S1(a)). Further increasing the H$_2$O content to 100 wt.% H$_2$O resulted in a decrease of mass activity to 140.4 mA·mg$_{Pt}^{-1}$. For MEA with different H$_2$O content, the ECSA value varied from 20.6 to 25.6 m^2·g$_{Pt}^{-1}$, which matched well with the trend of mass activities. The MEA with 90 wt.% H$_2$O delivered the largest ECSA value of 25.6 m^2·g$_{Pt}^{-1}$, which was much lower than that obtained in the RDE (64.0 m^2·g$_{Pt}^{-1}$, Figure S1(b)). This could be explained by the fact that part of the active sites (Pt surface areas) in the catalyst layer are not available for the electrochemical reaction due to either insufficient contact with the ionomer or electrical isolation of catalyst particles from each other by the thick film of non-electronic conductive ionomer.[26] The higher the ECSA value implies the more catalyst/ionomer interfaces (available active sites) throughout the catalyst layer.

Significant performance differences can be observed at low cell voltages (<0.8 V) in Figure 1(a). For better comparison, the current densities are plotted against H$_2$O content at different cell voltages in Figure 2(a). Except for the MEA fabricated with pure n-PA, the variation trends of current density with H$_2$O content basically followed the kinetic activity (Figure 1(c)). Although the MEA made with pure n-PA solvent exhibited the lowest kinetic activity (Figure 1(c)), its performance at high current density was better than the MEAs with 20 wt.% H$_2$O and 50 wt.%

H₂O (Figure 2(a)). This could be attributed to the different mass transport limitations of MEAs with different H₂O contents. Mass transport loss (η_{tx}) is mainly caused by the poor oxygen diffusion through the catalyst layer, especially when the fuel cell is operated at high current densities, which can be calculated from polarization curve based on the equation (1).[26]

$$E_{cell} = E_{rev} - iR_\Omega - \eta_{ORR} - \eta_{tx} \tag{1}$$

Here, E_{rev}, E_{cell}, and i are the reversible cell voltage, the measured cell voltage, and current density, respectively. The ohmic loss (iR_Ω) is caused by the ohmic resistances of cell components and contact resistances between the components, as seen in Figure 1(a), can be measured using current interrupt method. The kinetic overpotential (η_{ORR}) originates from the sluggish ORR kinetics on the cathode catalyst layer, which can be obtained from the Tafel equation ($\eta_{ORR} \propto b \log i$) derived from polarization curves at low current density region.[26-27] Figure 2(b) shows the derived voltage loss curves of the mass transport for different MEAs. The mass transport loss appreciably increased at higher current densities due to serious oxygen diffusion and water flooding issues. The variation in mass transport loss of different MEAs matched well with that observed in Figure 2(a), indicating the mass transport dominated the performance differences at high current densities. Mass transport resistances are closely related to the pore structure in the catalyst layer, because the reaction requires oxygen to be supplied to the catalyst particles through the pore channels. Appropriate pore structure in the catalyst layer is critical in facilitating oxygen diffusion and mitigating the water flooding issues.

To determine the H₂/air performances, the polarization and power density curves were measured, as shown in Figure 3(a). Compared with Figure 1(a), the MEA performances with air

were much lower. The peak power density varied from 737 to 919 mW·cm^{-2}, and the current

density at 0.6 V ranged from 914 to 1229 mA·cm^{-2}, with the alteration of H_2O content. The MEA

with 90 wt.% H_2O achieved the best performance, showing the highest peak power density of 919

mW·cm^{-2} and the largest current density of 1229 mA·cm^{-2} at 0.6 V. To analyze the H_2/air

performances given in Figure 3(a), the electrochemical impedance spectroscopies were collected

at 1.0 A·cm^{-2} from 10 kHz to 0.1 Hz, and fitted using an equivalent circuit described previously.[28]

The results are presented as Nyquist plots in Figure 3(b). In the inset equivalent circuit, R_Ω

represents the ohmic resistance arising from cell components and the contact resistance between

the components. R_{anode} and $R_{cathode}$ are Faradaic resistances, which reflect the kinetics of the

electrochemical reactions occurring on the anode and cathode sides, respectively. The constant

phase element (CPE) reflects the capacitive nature of the porous catalyst layer. The finite Warburg

circuit element (W_{mt}) is used to model the cathode mass transport. This model neglects any mass

transport loss arising from the anode, since the high flowrate of pure hydrogen used in this study

minimized this effect. Nyquist plots in Figure 3(a) show one impedance arc consisting of three

composite semicircles. As expected, the impedance arc shrank with the improvement of MEA

performance. The high frequency intercepts with the real axis in Nyquist plots are ohmic

resistances (R_Ω), which varied slightly for different MEAs. The fitted values of R_Ω are 73.8~77.5

mΩ·cm^2 for different MEAs. The impedance arcs at the high, medium and low frequency regions

are related to resistances of anode activation, cathode activation and mass transport, respectively.

The larger the arc, the greater the resistance of activation kinetics or mass transport. For all cases,

the anode related semicircles are almost masked by the cathode semicircles, indicating the

resistances of anode activation are significantly lower than that of cathode activation. The R_{anode} values slightly varied from 9.1 to 14.2 m$\Omega \cdot$cm^2 for different MEAs, due to the same anode catalyst layer were applied. To correlate the MEA performance with the impedance data, the P_{max} values from Figure 3(a), as well as the $R_{cathode}$ and R_{mt} values from Figure 3(b) are plotted against the H_2O contents in Figure 3(c). Obviously, the variation of $R_{cathode}$ values was consistent with that of ORR kinetics data (Figure 1(c)), and the variation of R_{mt} values matched well with that of mass transport data in Figure 2 (b). Except for the MEA fabricated with pure n-PA, the variations of $R_{cathode}$ and R_{mt} with H_2O content follow a similar trend. For the MEA with pure n-PA, the highest $R_{cathode}$ was compensated by the relatively low R_{mt} to some extent, leading to the improved performance as compared with 20 wt.% H_2O and 50 wt.% H_2O. Therefore, the H_2/air performance was jointly controlled by ORR kinetics and mass transport in the cathode. The $R_{cathode}$ values varied from 78.0 to 99.1 m$\Omega \cdot$cm^2, and R_{mt} values varied from 19.4 to 38.2 m$\Omega \cdot$cm^2, with the alteration of H_2O content. Both $R_{cathode}$ and R_{mt} reached the minimum values with 90 wt.% H_2O, resulted in the best performance.

To better understand how solvent composition affects MEA performance, the particle/aggregate sizes of ionomer and catalyst in different mixed solvents which determine the catalyst/ionomer interface needs to be studied. Varying the H_2O content of the n-PA/H_2O mixed solvents modifies the physical properties including polarizability (dielectric constant) and solubility, which govern the size and morphology of ionomer and catalyst particles/aggregates in the dispersing solvent. For better discussion, the dielectric constant, solubility and boiling point of different mixed solvents are compiled in Table II based on available literatures and database.[3, 29-]

[32] The ultrasmall angle x-ray scattering (USAXS) curves, scattered intensity (I) versus scattering vector (q), of the pure ionomer dispersions in different mixed solvents are shown in Figure 4(a). The scattering vector is reversely relative to particle size, and an increase in the scattered intensity at a given scattering vector indicates a larger population of particles at that size. As evident in Figure 4(a), the intensity signals at high q (>0.01 Å^{-1}) region were weak and noisy, indicating quite low populations of primary ionomer particles in mixed solvents, which was not considered in the following discussion. The scattering data at low q (<0.01 Å^{-1}) region was analyzed using a unified fitting mode with Porod and Guinier scattering regimes. The fitting results demonstrated the power-law slope of P = 4.0 with radius of gyration (R_g) from 61.1 to 85.0 nm for different mixed solvents, attributed to the formation of spherical ionomer aggregates. The average diameters of ionomer aggregates (twice the radius of gyration) are compared in Figure 4(c). For the ionomer dispersion, the average size of ionomer aggregates increased from 141.0 nm in pure n-PA (0 wt.% H_2O) to 170.0 nm in 50 wt.% H_2O, and then decreased appreciably to 122.2 nm in pure H_2O (100 wt.% H_2O). This variation trend is similar to the observation on Nafion ionomers in different i-PA/H_2O mixed solvents.(3) Due to the minimized difference between the solvent solubility and that of the sulfonate side chains, the mixed solvent of 50 wt.% H_2O has the highest compatibility with the sulfonate side chains of ionomer molecules. [3] For n-PA/H_2O mixed solvents, the dielectric constant increases with increasing the H_2O content, and the higher dielectric constant causes the ionomer molecules to dissociate more negatively charged $-SO_3^-$ groups from $-SO_3H$ groups.[3] Therefore, the resulted higher inter-polymer negative charge repulsions lead to smaller ionomer aggregates in the mixed solvents with a higher H_2O content (>50 wt.%). On the other hand, the

decreased size of ionomer aggregates with a lower H_2O content (<50 wt.%) could be attributed to the enhanced compatibility between the perfluorocarbon backbones and the mixed solvents containing more n-PA. In addition, the low-EW ionomer used in this study has more sulfonic acid groups and is therefore easier to disperse in H_2O-rich solvents compare with the traditional Nafion ionomer. This could explain the smallest size of ionomer aggregate in pure H_2O solvent. Previous studies reported that the smaller size of ionomer aggregates facilitated the ionomer infiltration inside the catalyst aggregates, resulting in better ionomer coverage on the catalyst surface and enhanced performance.[23-24] However, no such correlation between the ionomer size and MEA performance was observed in this study. This may be because the catalyst/ionomer interface is not only related to the size of ionomer aggregates, but also closely related to the dispersibility of the catalyst agglomerates. Effectively breaking the catalyst agglomerates into smaller aggregates is essential to enlarge the catalyst surface accessible to ionomers.

Figure 4(b) shows the scattering curves of the catalyst inks with different H_2O content. Several kneelike power-law regimes were observed in scattering curves, which correspond to the multilevel structures of carbon-ionomer agglomerates, aggregates, and Pt nanoparticles. The scattering differences between the inks are evident in the agglomerate regions (low q range, <0.001 Å^{-1}), while the differences in the aggregate and Pt nanoparticle regions (intermediate and high q range, respectively) appear to be not significant. However, the radius of gyration of the agglomerates cannot be determined directly from USAXS due to the knee of the agglomerate scattered beyond the measuring range. The slope of intensity in the low q region is proportional to the mass fractal dimension, which could be used to qualitatively characterize the extent of

agglomeration.[33-36] The larger slope implies the larger agglomerate size in the catalyst, and the more difficult it is for the agglomerate to break up into aggregate. The inset in Figure 4 (b) shows the zoomed-in low q region of the scattering profiles. Obviously, the slope decreased with increasing the H_2O content in the range of 0~90 wt.% H_2O, indicating the beneficial effect of more H_2O in reducing the agglomeration size, which agreed well with the observations on other inks such as PtNi/Vu and PtNi/HSC catalysts in n-PA/H_2O mixed solvents.[37] However, further increasing the H_2O content to 100 wt.% H_2O resulted in the largest slope, which could be attributed to the hydrophobic nature of pristine carbon particles. The size of Pt nanoparticles in different solvents remained almost unchanged, as the fitted average diameters in low q range slightly varied from 5.1 to 6.0 nm. The fitting results in intermediate q range show that the average diameters of the carbon-ionomer aggregates in different solvents varied from 262.8 to 290.6 nm, which followed a similar trend as observed in the agglomerate regions (low q range). The smaller sizes of catalyst-ionomer agglomerate/aggregate in the ink solvents are correlated reasonably well with the higher kinetic activities (mass activity and ECSA) in Figure 1(c). Although the smaller sizes of ionomer aggregate were achieved with pure n-PA and pure H_2O, the large sizes of catalyst agglomerate/aggregate reduce the catalyst surface accessible to ionomers, resulting in the lowest kinetic activities.

To validate the results from the USAXS data, cryo-TEM was used to visualize the aggregate sizes of ionomer and catalyst in the n-PA/H_2O mixed solvent with 90 wt.% H_2O. As evident in Figure 5(a), the ionomer aggregates exhibited a spherical geometry with a diameter of 100~200 nm, which is consistent with the average diameter of 139 nm obtained from USAXS fitting. The

structure of Nafion ionomer were extensively studied in various solvents previously.[3-10, 20, 38-40] At low ionomer concentrations, Nafion ionomers are known to exist as rod-like primary particles in H_2O-rich solvents or coil-like primary particles in alcohol-rich solvents.[38] The formation of rod-like primary particle in H_2O-rich solvents can be explained by the fact that sulfonic acid side chains are preferentially orient toward the solvent interface due to H_2O-rich solvents are more compatible with the sulfonic acid side chains than with the perfluorocarbon backbones.[3, 38] The rod-like structure with 2 nm in diameter and 20 nm in length was demonstrated using USAXS and cryo-TEM techniques.[38-39] The coil-like structure of ionomer primary particles was proposed with the perfluorocarbon backbones in contact with the alcohol-rich solvent and the sulfonic acid side chains buried inside the coiled structures.[3, 38] As ionomer concentration increased, the primary particles tend to form secondary aggregates via the inter-ionic interactions of side chain negatively charged $-SO_3^-$ groups with positively charged H_3O^+ ions or the inter-polymer perfluorocarbon backbone interactions.[3, 38] The aggregate structures of rod-like micelles and coil-like micelles were proposed in H_2O-rich and alcohol-rich solvents, respectively.[20, 38] Figure 5(b) shows a typical cryo-TEM image of catalyst-ionomer aggregates in the catalyst ink with 90 wt.% H_2O. For catalyst aggregates of carbon supported Pt nanoparticles, some sphere carbon particles aggregated to form a rod-like aggregate with a diameter/length around 300 nm, in consistent with the USAXS data. The ionomer aggregates appeared to be adsorbed on the surface of catalyst aggregates, which could be attributed to the van der Waals force between ionomer aggregates and catalyst aggregates. The interaction between ionomer and catalyst in the ink is critical to the formation of catalyst/ionomer interface in the catalytic layer.

The surface and cross-sectional morphologies of the catalyst layers with different solvents were examined, and the corresponding SEM images are given in Figure 6. Although the same catalyst and ionomer were used, the catalyst layers fabricated with different dispersing solvents exhibit apparently different microstructures. The catalyst layers with 20 wt.% H_2O and 50 wt.% H_2O had a relatively compact and smooth appearance, while the surface of other catalyst layers were rough and loose with obvious voids. Furthermore, large voids were observed for the catalyst layer fabricated with pure H_2O solvent. The catalyst layer with 90 wt.% H_2O (Figure S2) exhibited a spider web-like porous structure similar to that with pure H_2O, which is not shown in Figure 6 to simplify the description. Despite the difference in morphology, the thickness of all catalyst layers is 8~10 um due to the same catalyst and ionomer loadings.

The pore size distributions in the catalyst layers fabricated with different solvents on Nafion membranes were investigate using mercury intrusion porosimetry. The contribution of Nafion membrane to the total pore volumes is negligible since no mercury intrusion can be observed within the measuring range.[41] As evident in Figure 7 (a), the catalyst layers exhibited two distinctive pore size distributions with a critical boundary of 20 nm, in good agreement with those reported previously.[41-43] The primary pores in the range of 3~20 nm can be attributed to the void spaces inside and between the primary particles in the carbon aggregates, while the secondary pores (>20 nm) correspond to the void spaces between the carbon aggregates.[42-45] Obviously, the ionomer aggregates cannot infiltrate inside the primary pores because the ionomer aggregates (122.2~170.0 nm) are much larger than the primary pores (<20 nm). Therefore, the ionomer aggregates should be mainly distributed on the surface of catalyst aggregates covering the surface

of secondary pores, which act as ORR active sites due to the reaction requires the protons transport to the reaction sites to complete the conversion of oxygen to water. The specific volumes of the primary pores and secondary pores determined from Figure 7 (a) are compared in Figure 7 (b) and Table III. Both specific volumes of the primary and secondary pores first decreased with the increase of H_2O content, then increased to the maximum volumes, and then slightly decreased, which is very consistent with the variations of mass transport loss/resistance observed in Figure 2(b) and Figure 3(c). The lower mass transport loss/resistance could be directly linked to the larger specific pore volume, especially that of the secondary pores, which is critical in facilitating oxygen diffusion and mitigating the water flooding issues in improving the power density. The specific volume of the secondary pores reached the maximum values of 0.94 and 0.90 $cm^3 \cdot g^{-1}$ with 90 wt.% H_2O and 100 wt.% H_2O, respectively, resulting in the lowest mass transport losses. Previous studies attributed the higher specific pore volumes in the catalyst layer to the larger catalyst-ionomer aggregates/agglomerates in the catalyst ink.[19, 42] However, this is difficult to explain the changes in the pore structure observed in this study. In order to clarify the change of specific pore volume for different catalyst layers, the boiling points of different mixed solvents are compared in Figure 7 (b) and Table II according to the available database.[32] The boiling point of the mixed solvent varied from 87.8 °C to 100 °C with the alteration of H_2O content. Generally, a lower boiling point implies a higher evaporation rate at a given temperature. The mixed solvents with 20 wt.% H_2O and 50 wt.% H_2O are closest to the azeotropic composition of 28.8 wt.% H_2O (87.7 °C), resulting in the lowest boiling points. It should be noted that, for mixed solvents with a non-azeotropic composition, the boiling point gradually increases as the evaporation progresses due to

the changes in composition. As evident in Figure 7 (b), the specific pore volumes, especially that

of the secondary pores are closely related to the boiling points of the corresponding solvents. The

solvent with a higher boiling point (away from azeotropic composition) helps to form more

secondary pores. In this study, the catalyst layers were fabricated by directly ultrasonic spraying

the catalyst ink onto the Nafion membranes placed on a hot vacuum plate (<80 °C) without post-

drying or hot pressing. The microstructure of the catalyst layer was constructed during the solvent

evaporation, as a result of accumulation of the catalyst-ionomer aggregates. Due to the evaporation

of the dispersion solvents, the catalyst-ionomer aggregates in catalyst layer tend to form large

aggregates or agglomerates. For a low boiling point solvent, the solvent quickly evaporates, and

the mobility of the catalyst-ionomer aggregates is almost lost before the aggregates are packed

densely. In this case, the size of catalyst-ionomer aggregates in the catalyst ink determines the

pores structure of the ultimate catalyst layer, and the larger size of catalyst-ionomer aggregates in

the ink constructs the larger pores in the catalyst layer. However, for a high boiling point solvent

with a low evaporation rate, the catalyst-ionomer aggregates with a good mobility tends to

agglomerate together during the solvent evaporation to form larger catalyst-ionomer aggregates,

resulting in larger pores between the forming aggregates. The slower the solvent evaporation rate,

the more time it has to coagulate into larger aggregates to form more secondary pores, which is

similar to the process of evaporation-induced self-assembly.[46-48]

Above all, the composition of the n-PA/H_2O mixed solvents played a critical role on the

formation of the catalyst layer, and thus fuel cell performance. Varying the solvent composition

resulted in the change of physical properties including dielectric constant, solubility and boiling

point. The dielectric constant and solubility of each mixed solvent affect the aggregates (catalyst and ionomer) size in the catalyst ink, which ultimately determined the catalyst/ionomer interface (available active sites) of the resulting catalyst layer. The smaller aggregates in the catalyst ink facilitated the formation of a better catalyst/ionomer interface, resulting in enhanced kinetic activity (mass activity and ECSA). On the other hand, the boiling point was closely related to the solvent evaporation rate during the ultrasonic spraying process, which governed the pore structure of the catalyst layer. The dispersion solvent with a low evaporation rate appeared to be beneficial in forming secondary pores, which are critical in facilitating oxygen transport and mitigating the water flooding issues.

Conclusion

The MEA performances of a series of catalyst layers fabricated with catalyst inks using different solvent (n-PA/H_2O) composition in terms of H_2O content were investigated. The solvent composition demonstrated a strong influence on the structure and morphology of the catalyst layers, consequently, MEA performance on kinetic and mass-transport regions of the polarization curves. The catalyst layer fabricated with 90 wt.% H_2O demonstrated the best MEA performances because of the enhanced kinetic activity (mass activity and ECSA) and mass transport. The dispersions of catalyst powder and ionomer particles in different mixed solvent system were investigated using USAXS and cyro-TEM. The ionomer aggregates mainly covered on the surface of the catalyst aggregates acting as ORR active sites, since the size of ionomer aggregates were too large to infiltrate inside the catalyst aggregates. In the mixed solvents with 50~90 wt.% H_2O, the catalyst

agglomerates could be more effectively breakup into smaller aggregates, which enlarged catalyst/ionomer interface. The boiling point (evaporation rate) of the n-PA/H$_2$O mixed solvent determined the ultimate pore structure during catalyst layer fabrication. For a dispersing solvent with a high boiling point, the catalyst-ionomer aggregates tend to agglomerate during the solvent evaporation to form larger catalyst-ionomer aggregates, resulting in more secondary pores and thus lower mass transport resistance. The findings in this work will provide new insights on guiding the design of high-performance catalyst layer of PEM fuel cells.

References

1.   Uchida, M.; Aoyama, Y.; Eda, N.; Ohta, A., New Preparation Method for Polymer-Electrolyte Fuel Cells. *J. Electrochem. Soc.* **1995,** *142* (2), 463-468.

2.   Yang, F.; Xin, L.; Uzunoglu, A.; Stanciu, L.; Ilavsky, J.; Son, S.; Xie, J., Investigation of Solvent Effects on the Dispersion of Carbon Agglomerates and Nafion Ionomer Particles in Catalyst Inks Using Ultra Small Angle X-Ray Scattering Method. *ECS Trans.* **2016,** *75* (14), 361-371.

3.   Ngo, T. T.; Yu, T. L.; Lin, H.-L., Influence of the composition of isopropyl alcohol/water mixture solvents in catalyst ink solutions on proton exchange membrane fuel cell performance. *J. Power Sources* **2013,** *225*, 293-303.

4.   Ngo, T. T.; Yu, T. L.; Lin, H.-L., Nafion-based membrane electrode assemblies prepared from catalyst inks containing alcohol/water solvent mixtures. *J. Power Sources* **2013,** *238*, 1-10.

5.   Lee, S.-J.; Yu, T. L.; Lin, H.-L.; Liu, W.-H.; Lai, C.-L., Solution properties of nafion in methanol/water mixture solvent. *Polymer* **2004,** *45* (8), 2853-2862.

6.   Kim, T.-H.; Yi, J.-Y.; Jung, C.-Y.; Jeong, E.; Yi, S.-C., Solvent effect on the Nafion agglomerate morphology in the catalyst layer of the proton exchange membrane fuel cells. *Int. J. Hydrogen Energ.* **2017,** *42* (1), 478-485.

7.   Welch, C.; Labouriau, A.; Hjelm, R.; Orler, B.; Johnston, C.; Kim, Y. S., Nafion in Dilute Solvent Systems: Dispersion or Solution? *ACS Macro Lett.* **2012,** *1* (12), 1403-1407.

8.   Johnston, C. M.; Lee, K.-S.; Rockward, T.; Labouriau, A.; Mack, N.; Kim, Y. S., Impact of Solvent on Ionomer Structure and Fuel Cell Durability. *ECS Trans.* **2009,** *25* (1), 1617-1622.

9.   Ma, C.-H.; Yu, T. L.; Lin, H.-L.; Huang, Y.-T.; Chen, Y.-L.; Jeng, U. S.; Lai, Y.-H.; Sun, Y.-S., Morphology and properties of Nafion membranes prepared by solution casting. *Polymer* **2009,** *50* (7), 1764-1777.

10. Wang, Z.; Tang, H.; Li, J.; Zeng, Y.; Chen, L.; Pan, M., Insight into the structural construction of a perfluorosulfonic acid membrane derived from a polymeric dispersion. *J. Power Sources* **2014,** *256*, 383-393.

11. Shin, S. J.; Lee, J. K.; Ha, H. Y.; Hong, S. A.; Chun, H. S.; Oh, I. H., Effect of the catalytic ink preparation method on the performance of polymer electrolyte membrane fuel cells. *J. Power Sources* **2002,** *106* (1-2), 146-152.

12. Fernández, R.; Ferreira-Aparicio, P.; Daza, L., PEMFC electrode preparation: Influence of the solvent composition and evaporation rate on the catalytic layer microstructure. *J. Power Sources* **2005,** *151*, 18-24.

13. Yang, T.-H.; Yoon, Y.-G.; Park, G.-G.; Lee, W.-Y.; Kim, C.-S., Fabrication of a thin catalyst layer using organic solvents. *J. Power Sources* **2004,** *127* (1-2), 230-233.

14. Huang, D.; Yu, P.; Liu, F.; Huang, S.; Hsueh, K.; Chen, Y.; Wu, C.; Chang, W.; Tsau, F., Effect of Dispersion Solvent in Catalyst Ink on Proton Exchange Membrane Fuel Cell Performance. *Int. J. Electrochem. Sc.* **2011,** *6* (7), 2551-2565

15. Therdthianwong, A.; Ekdharmasuit, P.; Therdthianwong, S., Fabrication and Performance of Membrane Electrode Assembly Prepared by a Catalyst-Coated Membrane Method: Effect of Solvents Used in a Catalyst Ink Mixture. *Energy Fuels* **2010,** *24* (2), 1191-1196.

16. Yang, D.; Yu, H.; Li, G.; Zhao, Y.; Liu, Y.; Zhang, C.; Song, W.; Shao, Z., Fine microstructure

of high performance electrode in alkaline anion exchange membrane fuel cells. *J. Power Sources* **2014,** *267*, 39-47.

17. Zhao, J.; Li, X.; Liu, Z. s., The effect of ink dilution and evaporation on the microstructures of catalyst layers in polymer electrolyte membrane fuel cells.   *Int. J. Energy Res.* **2019**.

18. Zhang, J.; Pei, Y.; Zhu, W.; Liu, Y.; Yin, Y.; Qin, Y.; Guiver, M. D., Ionomer dispersion solvent influence on the microstructure of Co–N–C catalyst layers for anion exchange membrane fuel cell. *J. Power Sources* **2021,** *484*.

19. Osmieri, L.; Wang, G.; Cetinbas, F. C.; Khandavalli, S.; Park, J.; Medina, S.; Mauger, S. A.; Ulsh, M.; Pylypenko, S.; Myers, D. J.; Neyerlin, K. C., Utilizing ink composition to tune bulk-electrode gas transport, performance, and operational robustness for a Fe–N–C catalyst in polymer electrolyte fuel cell. *Nano Energy* **2020,** *75*.

20. Khandavalli, S.; Iyer, R.; Park, J. H.; Myers, D. J.; Neyerlin, K. C.; Ulsh, M.; Mauger, S. A., Effect of Dispersion Medium Composition and Ionomer Concentration on the Microstructure and Rheology of Fe-N-C Platinum Group Metal-free Catalyst Inks for Polymer Electrolyte Membrane Fuel Cells. *Langmuir* **2020,** *36* (41), 12247-12260.

21. Van Cleve, T.; Khandavalli, S.; Chowdhury, A.; Medina, S.; Pylypenko, S.; Wang, M.; More, K. L.; Kariuki, N.; Myers, D. J.; Weber, A. Z.; Mauger, S. A.; Ulsh, M.; Neyerlin, K. C., Dictating Pt-Based Electrocatalyst Performance in Polymer Electrolyte Fuel Cells, from Formulation to Application. *ACS Appl. Mater. Interfaces* **2019,** *11* (50), 46953-46964.

22. Takahashi, S.; Mashio, T.; Horibe, N.; Akizuki, K.; Ohma, A., Analysis of the Microstructure Formation Process and Its Influence on the Performance of Polymer Electrolyte Fuel-Cell Catalyst

Layers. *ChemElectroChem* **2015,** *2* (10), 1560-1567.

23. Orfanidi, A.; Rheinländer, P. J.; Schulte, N.; Gasteiger, H. A., Ink Solvent Dependence of the Ionomer Distribution in the Catalyst Layer of a PEMFC. *J. Electrochem. Soc.* **2018,** *165* (14), F1254-F1263.

24. Xie, Z.; Navessin, T.; Zhao, X.; Adachi, M.; Holdcroft, S.; Mashio, T.; Ohma, A.; Shinohara, K., Nafion Ionomer Aggregation and its Influence on Proton Conduction and Mass Transport in Fuel Cell Catalyst Layers. *ECS Trans.* **2008,** *16* (2), 1811-1816.

25. Park, Y.-C.; Kakinuma, K.; Uchida, H.; Watanabe, M.; Uchida, M., Effects of short-side-chain perfluorosulfonic acid ionomers as binders on the performance of low Pt loading fuel cell cathodes. *J. Power Sources* **2015,** *275*, 384-391.

26. Gasteiger, H. A.; Kocha, S. S.; Sompalli, B.; Wagner, F. T., Activity benchmarks and requirements for Pt, Pt-alloy, and non-Pt oxygen reduction catalysts for PEMFCs. *Appl. Catal. B* **2005,** *56* (1-2), 9-35.

27. Xie, J.; Xu, F.; Wood, D. L.; More, K. L.; Zawodzinski, T. A.; Smith, W. H., Influence of ionomer content on the structure and performance of PEFC membrane electrode assemblies. *Electrochim. Acta* **2010,** *55* (24), 7404-7412.

28. O'Hayre, R.; Cha, S.-W.; Colella, W.; Prinz, F. B., Chapter 7: Fuel Cell Characterization. In *Fuel Cell Fundamentals*, 2016; pp 237-270.

29. Sato, T.; Chiba, A.; Nozaki, R., Composition-dependent dynamical structures of 1-propanol–water mixtures determined by dynamical dielectric properties. *J. Chem. Phys.* **2000,** *113* (21), 9748-9758.

30. Yeo, R. S., Dual cohesive energy densities of perfluorosulphonic acid (Nafion) membrane. *Polymer* **1980,** *21* (4), 432-435.

31. Moore, R. B.; Martin, C. R., Chemical and morphological properties of solution-cast perfluorosulfonate ionomers. *Macromolecules* **1988,** *21* (5), 1334-1339.

32. 1-Propanol-Water Vapor-Liquid Equilibrium: Datasheet from "Dortmund Data Bank (DDB) – Thermophysical Properties Edition 2014" in SpringerMaterials (https://materials.springer.com/thermophysical/docs/vle_c140c174), Springer-Verlag Berlin Heidelberg & DDBST GmbH, Oldenburg, Germany.

33. Beaucage, G., Small-Angle Scattering from Polymeric Mass Fractals of Arbitrary Mass-Fractal Dimension. *J. Appl. Crystallogr.* **1996,** *29* (2), 134-146.

34. Andrews, R. N.; Serio, J.; Muralidharan, G.; Ilavsky, J., An in situ USAXS-SAXS-WAXS study of precipitate size distribution evolution in a model Ni-based alloy. *J. Appl. Crystallogr.* **2017,** *50* (Pt 3), 734-740.

35. Khandavalli, S.; Park, J. H.; Kariuki, N. N.; Myers, D. J.; Stickel, J. J.; Hurst, K.; Neyerlin, K. C.; Ulsh, M.; Mauger, S. A., Rheological Investigation on the Microstructure of Fuel Cell Catalyst Inks. *ACS Appl. Mater. Interfaces* **2018,** *10* (50), 43610-43622.

36. Wang, M.; Park, J. H.; Kabir, S.; Neyerlin, K. C.; Kariuki, N. N.; Lv, H.; Stamenkovic, V. R.; Myers, D. J.; Ulsh, M.; Mauger, S. A., Impact of Catalyst Ink Dispersing Methodology on Fuel Cell Performance Using in-Situ X-ray Scattering. *ACS Appl. Energy Mater.* **2019,** *2* (9), 6417-6427.

37. Borup, R.; Weber, A., FC-PAD: Fuel Cell Performance and Durability Consortium. *Annual Merit Review* **2020**.

38. Berlinger, S. A.; McCloskey, B. D.; Weber, A. Z., Inherent Acidity of Perfluorosulfonic Acid Ionomer Dispersions and Implications for Ink Aggregation. *J. Phys. Chem. B* **2018,** *122* (31), 7790-7796.

39. Xu, F.; Zhang, H.; Ilavsky, J.; Stanciu, L.; Ho, D.; Justice, M. J.; Petrache, H. I.; Xie, J., Investigation of a catalyst ink dispersion using both ultra-small-angle X-ray scattering and cryogenic TEM. *Langmuir* **2010,** *26* (24), 19199-208.

40. Kim, Y. S.; Welch, C. F.; Hjelm, R. P.; Mack, N. H.; Labouriau, A.; Orler, E. B., Origin of Toughness in Dispersion-Cast Nafion Membranes. *Macromolecules* **2015,** *48* (7), 2161-2172.

41. Xin, L.; Yang, F.; Qiu, Y.; Uzunoglu, A.; Rockward, T.; Borup, R. L.; Stanciu, L. A.; Li, W.; Xie, J., Polybenzimidazole (PBI) Functionalized Nanographene as Highly Stable Catalyst Support for Polymer Electrolyte Membrane Fuel Cells (PEMFCs). *J. Electrochem. Soc.* **2016,** *163* (10), F1228-F1236.

42. Xin, L.; Yang, F.; Xie, J.; Yang, Z.; Kariuki, N. N.; Myers, D. J.; Peng, J.-K.; Wang, X.; Ahluwalia, R. K.; Yu, K.; Ferreira, P. J.; Bonastre, A. M.; Fongalland, D.; Sharman, J., Enhanced MEA Performance for PEMFCs under Low Relative Humidity and Low Oxygen Content Conditions via Catalyst Functionalization. *J. Electrochem. Soc.* **2017,** *164* (6), F674-F684.

43. Xie, J.; More, K. L.; Zawodzinski, T. A.; Smith, W. H., Porosimetry of MEAs Made by "Thin Film Decal" Method and Its Effect on Performance of PEFCs. *J. Electrochem. Soc.* **2004,** *151* (11).

44. Uchida, M.; Fukuoka, Y.; Sugawara, Y.; Ohara, H.; Ohta, A., Improved Preparation Process of Very-Low-Platinum-Loading Electrodes for Polymer Electrolyte Fuel Cells. *J. Electrochem. Soc.* **1998,** *145* (11), 3708-3713.

45. Uchida, M.; Aoyama, Y.; Eda, N.; Ohta, A., Investigation of the Microstructure in the Catalyst Layer and Effects of Both Perfluorosulfonate Ionomer and PTFE-Loaded Carbon on the Catalyst Layer of Polymer Electrolyte Fuel Cells. *J. Electrochem. Soc.* **2014,** *142* (12), 4143-4149.

46. Xie, Y.; Guo, S.; Guo, C.; He, M.; Chen, D.; Ji, Y.; Chen, Z.; Wu, X.; Liu, Q.; Xie, S., Controllable two-stage droplet evaporation method and its nanoparticle self-assembly mechanism. *Langmuir* **2013,** *29* (21), 6232-41.

47. Josten, E.; Wetterskog, E.; Glavic, A.; Boesecke, P.; Feoktystov, A.; Brauweiler-Reuters, E.; Rucker, U.; Salazar-Alvarez, G.; Bruckel, T.; Bergstrom, L., Superlattice growth and rearrangement during evaporation-induced nanoparticle self-assembly. *Sci. Rep.* **2017,** *7* (1), 2802.

48. Sahu, P.; Prasad, B. L. V., Dilution does the trick: Role of mixed solvent evaporation in controlling nanoparticle self-assembly. *Colloids Surf. A Physicochem. Eng. Asp.* **2014,** *447*, 142-147.

Table I. Performance parameters of the MEAs fabricated with different n-PA/H_2O mixed solvents

H_2O Content (wt.%)	Mass activity (mA·mg$_{Pt}^{-1}$)	Current density at 0.6 V (H_2/air, mA·cm^{-2})	Peak power density (H_2/air, mW·cm^{-2})	ECSA (m^2·g^{-1})	Tafel slope (mV·dec^{-1})
0	140.5	1032	781	20.6	63.9
20%	140.2	914	737	22.6	71.0
50%	154.6	918	770	22.9	69.8
70%	174.9	1035	797	23.8	66.1
90%	189.4	1229	919	25.6	68.3
100%	140.4	1158	858	21.5	65.8

Table II. Physical parameters of different n-PA/H_2O mixed solvents.

H_2O Content (wt.%)	Dielectric constant	Solubility	Boiling point (°C)
0	20	11.9	97.2
20%	25	14.4	87.8
50%	44	17.9	88.0
70%	58	20.1	88.4
90%	73	22.3	93.3
100%	78	23.4	100.0
Ionomer		9.7 (backbone)	
		17.3 (side chain)	

Table III. Porosimetry properties of the catalyst layers fabricated with different n-PA/H$_2$O mixed solvents

H$_2$O Content (wt.%)	Primary pore		Secondary pore	
	Pore range (nm)	Pore volume (cm^3·g^{-1})	Pore range (nm)	Pore volume (cm^3·g^{-1})
0	< 20	0.47	20~400	0.64
20%	< 20	0.30	20~108	0.39
50%	< 20	0.10	20~340	0.41
70%	< 20	0.33	20~1000	0.57
90%	< 20	0.35	20~1000	0.94
100%	< 20	0.21	20~1000	0.90
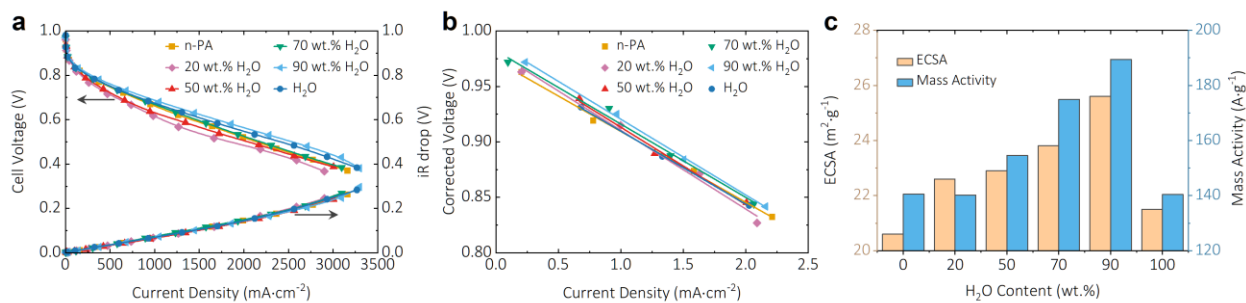
Figure 1. (a) H_2/O_2 polarization curves and (b) the corresponding Tafel plots of MEAs fabricated with different n-PA/H_2O mixed solvents. Testing conditions: H_2/O_2 (200/400 sccm), 80 °C, 100% RH, 150 kPa (absolute) backpressure. (c) Comparison of electrochemical surface area (ECSA) and mass activity at 0.9 $V_{iR-free}$.
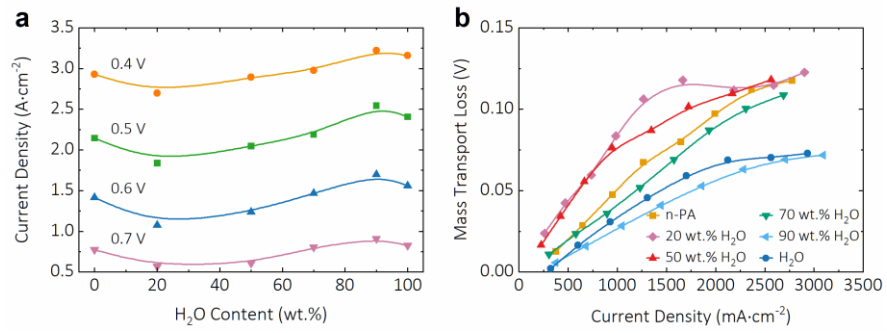
Figure 2. (a) Current density as a function of H_2O content in the mixed solvents plotted at different voltages. (b) Mass transport loss of MEAs fabricated with different n-PA/H_2O mixed solvents. The data presented here are derived from the data in Figure 1.
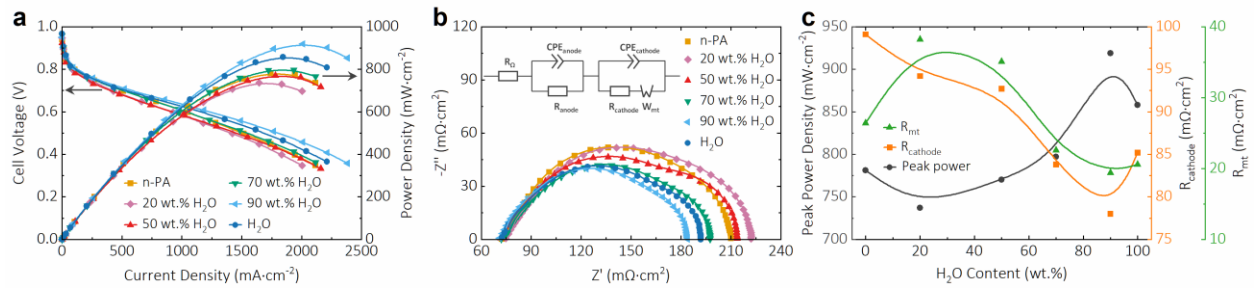
Figure 3. (a) H_2/air polarization and power density curves of MEAs fabricated with different n-PA/H_2O mixed solvents. Test conditions: H_2/air (500/2000 sccm), 80 °C, 100% RH, 150 kPa (absolute) backpressure. (b) Nyquist plots obtained at 1.0 A·cm^{-2} from 0.1 Hz to 10 kHz in the corresponding H_2/air fuel cell tests. The symbols are measured data, while the solid lines are fitted data using the inset equivalent circuit. (c) Variations of the cathode resistance ($R_{cathode}$), mass transport resistance (R_{mt}) and peak power density with H_2O content in the n-PA/H_2O mixed solvents.
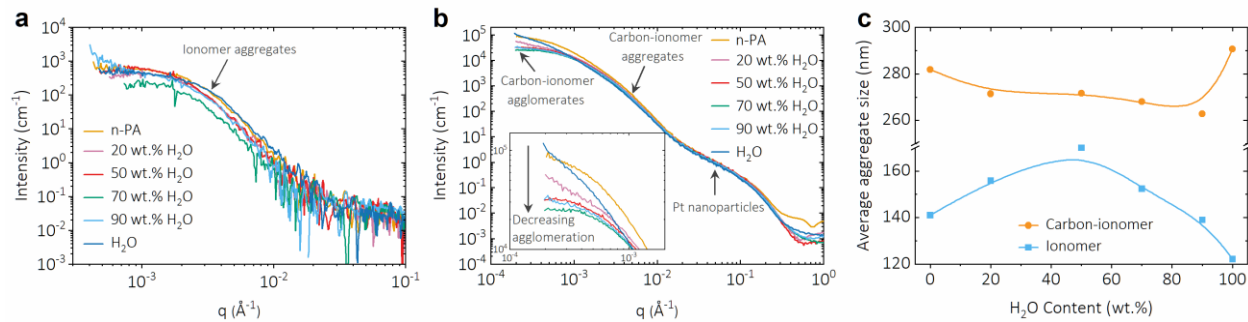
Figure 4. USAXS curves of (a) ionomer solutions and (b) catalyst inks for different n-PA/H$_2$O mixed solvents. The inset in (b) shows a zoomed-in low-*q* region. (c) USAXS fitted average sizes of ionomer aggregates and catalyst-ionomer aggregates.
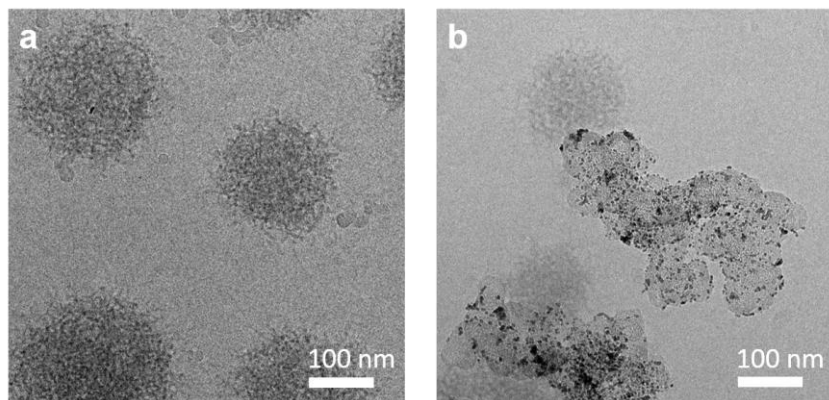
Figure 5. Cryo-TEM images of (a) ionomer and (b) catalyst-ionomer dispersed in the n-PA/H$_2$O mixed solvent containing 90 wt.% H$_2$O. The here used concentrations of ionomer and catalyst are equivalent to these used in the catalyst inks.
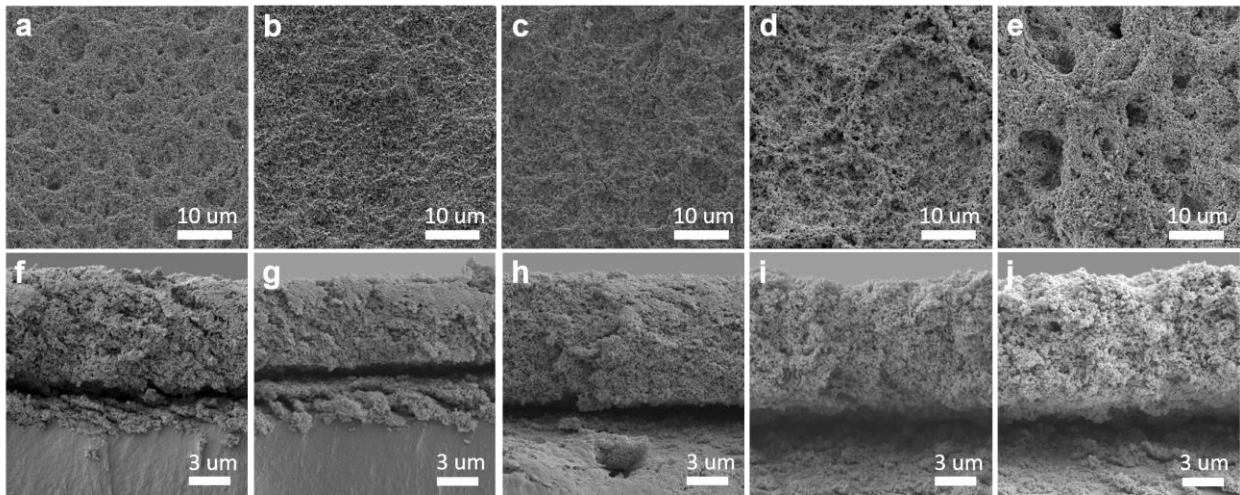
Figure 6. Top-view (a-e) and cross-sectional (f-j) SEM images of the catalyst layers fabricated with different n-PA/H_2O mixed solvents. (a, f) n-PA; (b, g) 20 wt.% H_2O; (c, h) 50 wt.% H_2O; (d, i) 70 wt.% H_2O; (e, j) H_2O.
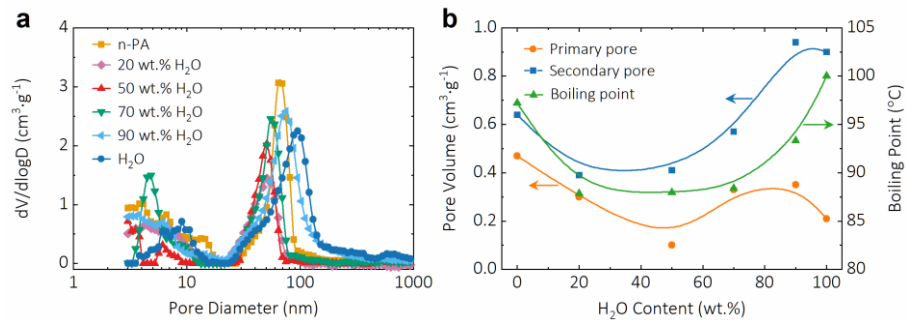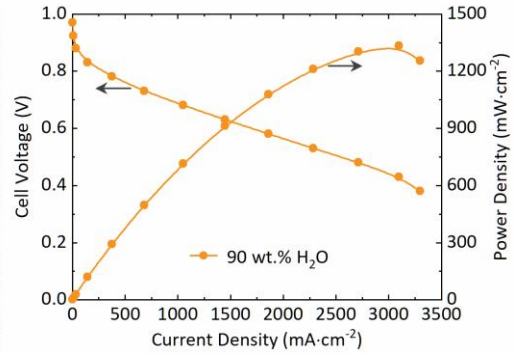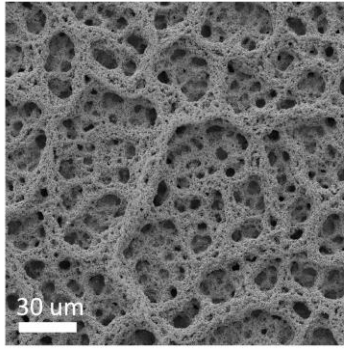
Figure 7. (a) Specific pore volume distribution curves of the catalyst layers fabricated with different n-PA/H_2O mixed solvents. (b) Variations of the specific volumes of primary pore and secondary pore, as well as the boiling point with H_2O content in the mixed solvents.

TOC

Supporting Information

Effects of Ink Formulation on Constructing Catalyst Layers

for High-Performance PEM Fuel Cells

Qing Gong[1,2], Chenzhao Li[1,3], Jan Ilavsky[4], Fei Guo[5], Xuan Cheng[2]*, Jian Xie[1]*

[1] Department of Mechanical Engineering, Purdue School of Engineering and Technology, Indiana University-Purdue University, Indianapolis, Indiana 46202, USA. Email: jianxie@iupui.edu

[2] Department of Materials Science and Engineering, College of Materials, Xiamen University, Xiamen, Fujian 361005, China. E-mail: xcheng@xmu.edu.cn

[3] School of Mechanical Engineering, Purdue University, West Lafayette, Indiana 47906, USA

[4] X-Ray Science Division, Argonne National Laboratory, Lemont, Illinois 60439, USA

[5] Department of Molecular and Cellular Biology, University of California, Davis, Davis, CA 95616-8665, USA
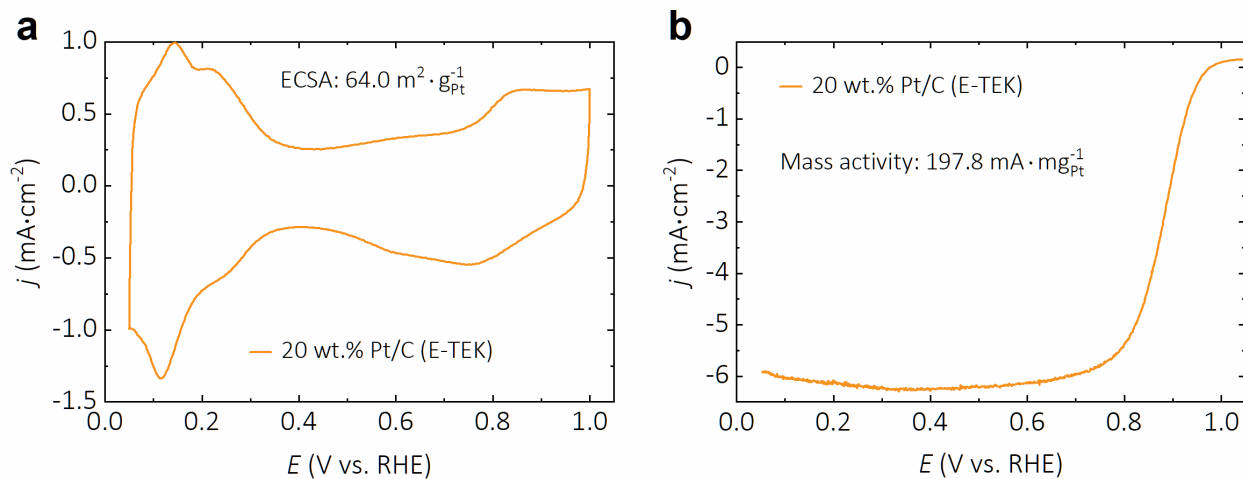
Figure S1. Electrocatalytic activities of the commercial 20 wt.% Pt/C (E-TEK) catalyst. (a) CV curves in N_2 saturated 0.1 mol·L^{-1} $HClO_4$ solution at 50 mV·s^{-1}. (b) RDE polarization curves in O_2 saturated 0.1 mol·L^{-1} $HClO_4$ solution at 10 mV·s^{-1} and 1600 rpm.
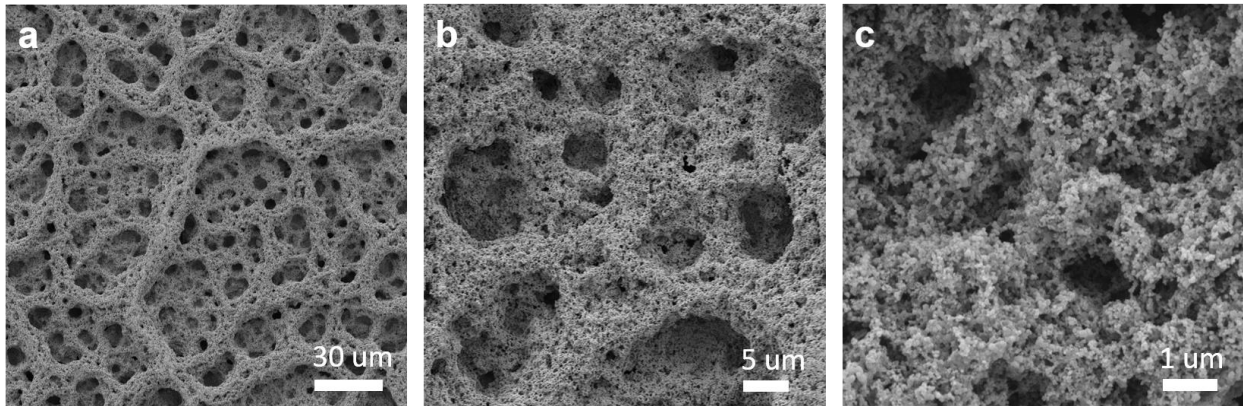
Figure S2. Top-view SEM images of the catalyst layer fabricated with the n-PA/H_2O mixed solvent containing 90 wt.% H_2O.